

Melimine-Modified 3D-Printed Polycaprolactone Scaffolds for the Prevention of Biofilm-Related Biomaterial Infections

Silvia Cometta, Robert T. Jones, Alfredo Juárez-Saldivar, Bogdan C. Donose, Muhammad Yasir, Nathalie Bock, Tim R. Dargaville, Karl Bertling, Michael Brüning, Aleksandar D. Rakić, Mark Willcox, and Dietmar W. Hutmacher*



Cite This: *ACS Nano* 2022, 16, 16497–16512



Read Online

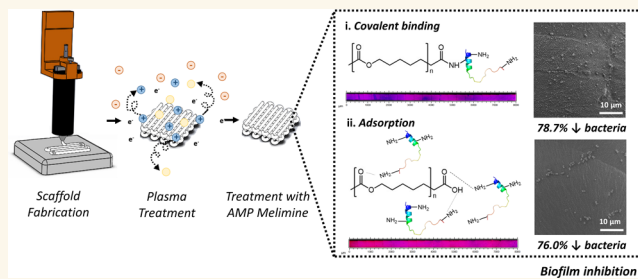
ACCESS |

Metrics & More

Article Recommendations

Supporting Information

ABSTRACT: Biomaterial-associated infections are one of the major causes of implant failure. These infections result from persistent bacteria that have adhered to the biomaterial surface before, during, or after surgery and have formed a biofilm on the implant's surface. It is estimated that 4 to 10% of implant surfaces are contaminated with bacteria; however, the infection rate can be as high as 30% in intensive care units in developed countries and as high as 45% in developing countries. To date, there is no clinical solution to prevent implant infection without relying on the use of high doses of antibiotics supplied systemically and/or removal of the infected device. In this study, melimine, a chimeric cationic peptide that has been tested in Phase I and II human clinical trials, was immobilized onto the surface of 3D-printed medical-grade polycaprolactone (mPCL) scaffolds via covalent binding and adsorption. X-ray photoelectron spectroscopy (XPS) and time-of-flight secondary ion mass spectrometry (ToF-SIMS) spectra of melimine-treated surfaces confirmed immobilization of the peptide, as well as its homogeneous distribution throughout the scaffold surface. Amino acid analysis showed that melimine covalent and noncovalent immobilization resulted in a peptide density of ~ 156 and ~ 533 ng/cm², respectively. Furthermore, we demonstrated that the immobilization of melimine on mPCL scaffolds by 1-ethyl-3-[3-(dimethylamino)propyl] carbodiimide hydrochloride (EDC) coupling and noncovalent interactions resulted in a reduction of *Staphylococcus aureus* colonization by 78.7% and 76.0%, respectively, in comparison with the nonmodified control specimens. Particularly, the modified surfaces maintained their antibacterial properties for 3 days, which resulted in the inhibition of biofilm formation *in vitro*. This system offers a biomaterial strategy to effectively prevent biofilm-related infections on implant surfaces without relying on the use of prophylactic antibiotic treatment.



KEYWORDS: bacterial infection, antimicrobial peptide, polycaprolactone, 3D printing, scaffold, melimine

1. INTRODUCTION

Biomaterial-associated infections are one of the major causes of implant failure.¹ On average, 4% to 10% of implant surfaces are estimated to be contaminated with bacteria; however, the infection rate can be as high as 30% in intensive care units in developed countries, and as high as 45% in developing countries.² In spite of efforts to maintain sterility during surgery, the operating theater is never truly sterile. Airborne particles carrying pathogens agglomerate on the surgical site because of door openings and movement of the medical personnel, thereby decreasing the efficiency of ultraclean ventilation systems.^{3,4} Patients could also be a source of contamination as bacteria residing in deeper skin layers, and

that are not accessible to regular disinfection, might come in contact with the implant during surgery.¹

Upon contact with implants, bacteria can rapidly colonize the surface and form a biofilm. Once in this state, bacteria become 10 to 1000 times more resistant to the host immune response and antimicrobial agents.⁵ The gold standard treatment to prevent implant-related infections is the systemic

Received: June 13, 2022

Accepted: September 28, 2022

Published: October 17, 2022



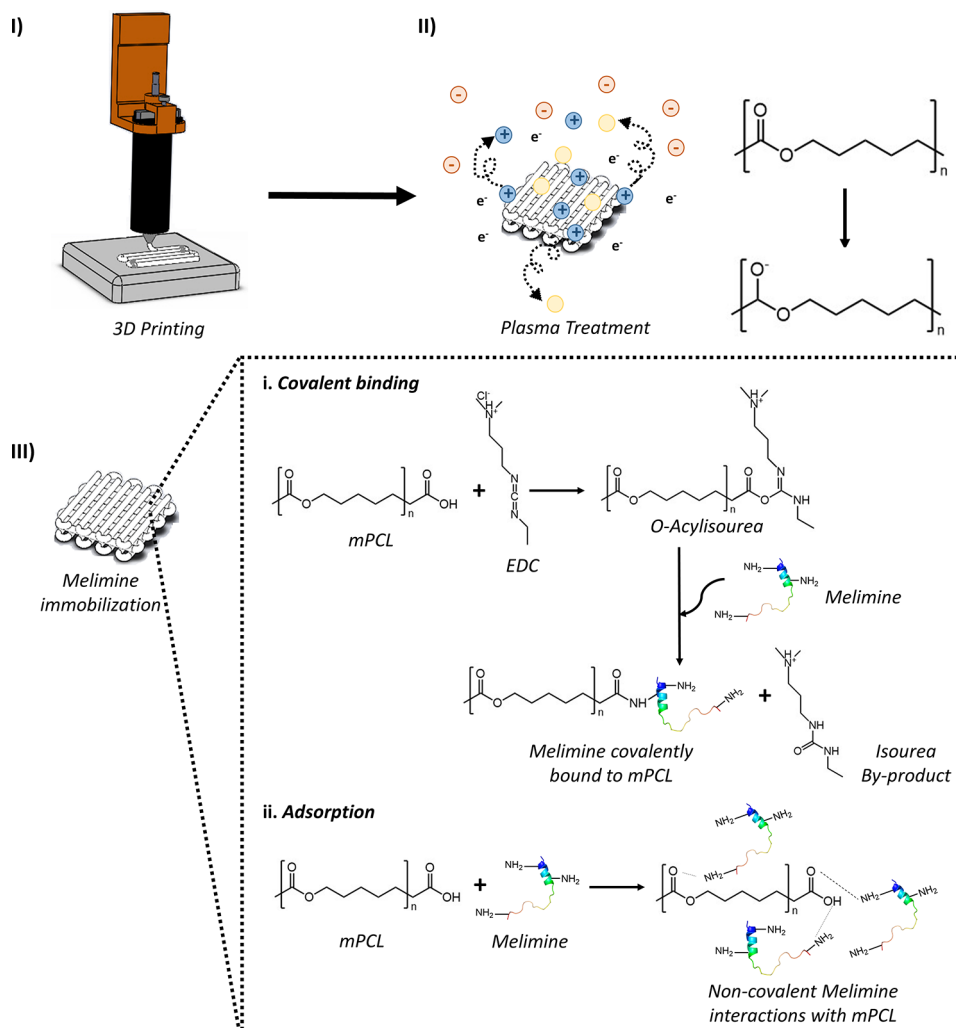


Figure 1. Schematic illustration of the steps of mPCL surface modification: (I) 3D printing, (II) plasma treatment (Ar and O₂), and (III) melimine-immobilization through (i) covalent binding via EDC coupling and (ii) adsorption via noncovalent interactions that are represented as dotted lines.

administration of antibiotics perioperatively; nevertheless, conventional administration of antibiotics has several side effects for the patient. Additionally, the increasing emergence of antibiotic-resistant bacteria strains has further impaired the efficacy of antibiotics. As an example, about 40% of *Staphylococcus epidermidis* and 32% of *Staphylococcus aureus* species isolated from orthopedic postsurgical and implant-related infections have been found resistant to gentamicin.^{6,7}

An alternative to prevent bacterial colonization on implants is making the implant surface antimicrobial. This can be achieved by immobilizing agents with antimicrobial properties. The choice of the antibacterial agent to be immobilized is vital to ensure the stability, efficacy, and safety of the modified biomaterial. Ideal clinically effective antimicrobial agents, rather than traditional antibiotics, need to have a wide spectrum of activity at low concentrations, be stable, and most importantly, antimicrobials should have a reduced or no probability of resistance evolution.^{8,9}

Antimicrobial peptides (AMPs) have emerged as a promising alternative to combat a broad spectrum of multidrug-resistant and persistent bacteria as they have been shown to be able to successfully prevent bacteria adhesion to biomaterials, to kill bacteria residing within biofilms, and to

rupture the biofilm structure.^{10–13} Only a few studies have aimed to immobilize AMPs within and on polycaprolactone (PCL) scaffolds; most of these studies developed AMP-releasing PCL electrospun scaffolds by blending the polymer solution with different concentrations of AMPs before scaffold manufacturing.^{14,15} Another study has incorporated AMP blends within PCL fibers by using coaxial electrospinning.¹⁶ Nevertheless, to the best of our knowledge, there are no studies investigating the immobilization of AMPs on medical-grade PCL (mPCL) scaffolds via covalent binding or adsorption.

In this study, melimine, a chimeric cationic peptide that has been tested in Phase I and II human clinical trials,¹⁷ is immobilized onto the surface of 3D printed mPCL scaffolds by covalent binding via 1-ethyl-3-[3-(dimethylamino)propyl] carbodiimide hydrochloride (EDC) coupling as well as by adsorption through noncovalent interactions (Figure 1). The modified surfaces are thoroughly characterized by a combination of state-of-the-art techniques such as nanoscale Fourier transform infrared spectroscopy (nanoFTIR), time-of-flight secondary ion mass spectrometry (ToF-SIMS), and quartz crystal microbalance (QCM). In addition, the ability of

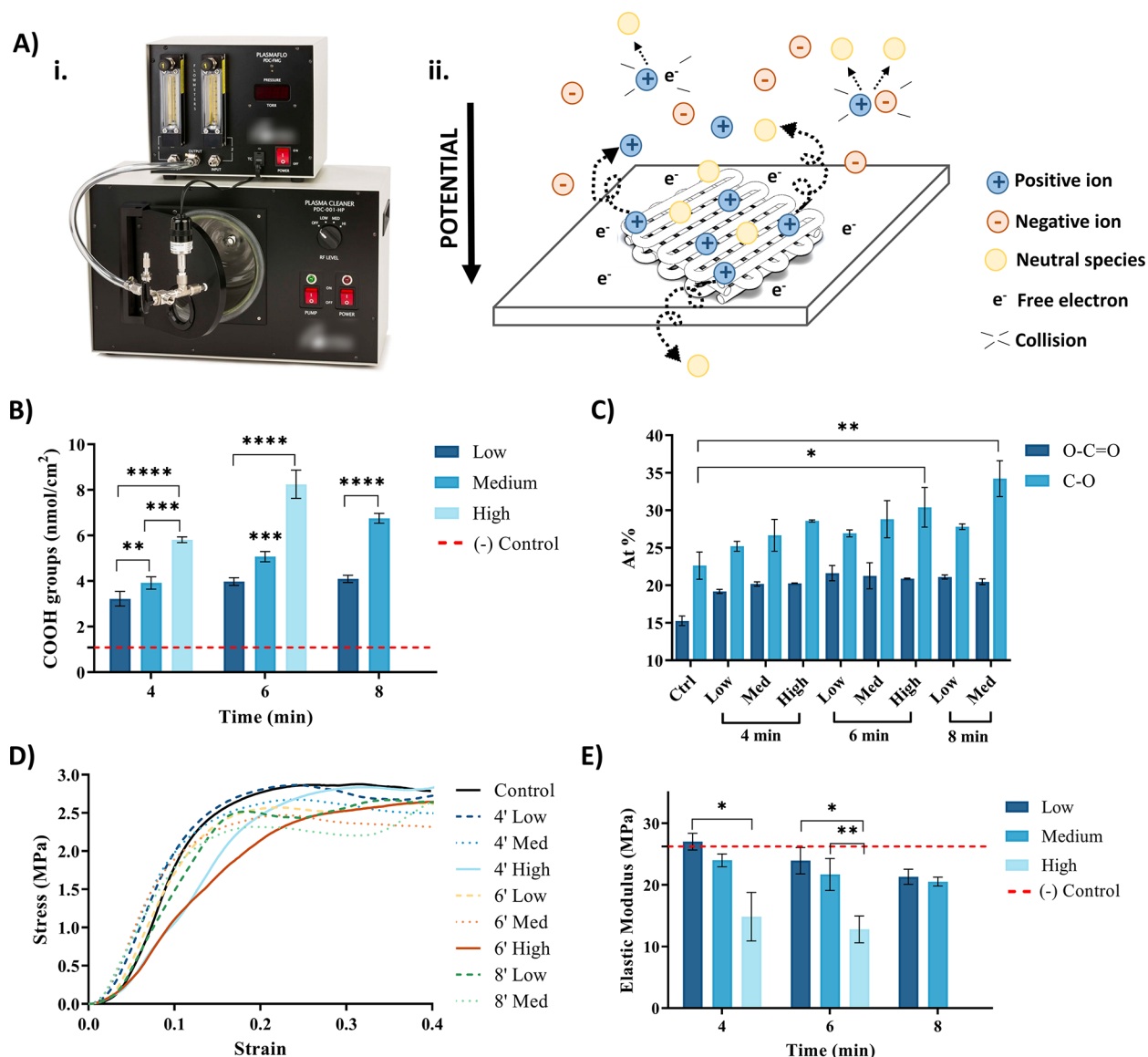


Figure 2. Characterization of surface chemistry and mechanical properties of mPCL scaffolds after plasma treatment at different power levels and exposure times. (A, i) Commercial plasma cleaner used for the treatment and (ii) schematic representation of the interactions between plasma species and the mPCL scaffold surface. (B) Carboxyl group density on untreated (red dotted line) and treated surfaces. (C) Deconvoluted high-resolution XPS spectra of C 1s showing the relative concentration of oxygen-containing functional groups after surface treatment. (D) Stress–strain curves and (E) elastic modulus (MPa) of pristine (red dotted line) and plasma-modified scaffolds exposed to uniaxial compression testing. All measurements are reported as average \pm standard deviation (SD); * $p < 0.05$, ** $p < 0.01$, *** $p < 0.001$, **** $p < 0.0001$ ($n = 4$).

melimine-modified surfaces to prevent *S. aureus* bacteria adhesion and biofilm formation for 3 days *in vitro* is assessed.

2. RESULTS AND DISCUSSION

2.1. mPCL Surface Modification Increases Reactive Groups for Melimine Immobilization.

Aliphatic polyesters such as mPCL have a characteristically low surface energy and limited chemical reactivity that restrict the coupling of active biomolecules such as AMPs.¹⁸ Herein, we use O₂ and Ar plasma treatment to oxidize ester groups present on the mPCL surface to form carboxylic groups that can then be used for the covalent coupling of the antimicrobial peptide melimine. Scaffolds were exposed to plasma for 4, 6, and 8 min at different power levels (low, medium, and high) in order to determine the optimal surface treatment conditions that lead

to the highest density of carboxylic groups on the surface without compromising the mechanical properties of the scaffolds.

Figure 2Aii) illustrates the process of plasma-treating the mPCL scaffolds. Gaseous plasma generated during the surface treatment is composed of positively and negatively charged ions, free electrons (e⁻), and neutral species. Once the surface is exposed to plasma, free electrons, which are considerably faster than the other species, diffuse quickly toward the material surface, thereby leaving the much slower ions in the plasma and, hence, creating a potential gradient between the plasma and the surface.¹⁹ This potential difference does not affect neutral species, so these move randomly until they eventually reach the material surface. Negatively charged ions, however, are affected by the resulting electrical field and are

sent back into the gaseous plasma before they are able to reach the surface. By comparison, positively charged ions, which are responsible for the surface modification, move randomly at similar velocities to the neutral species until they approach the surface, at which point the attracting potential accelerates them toward the material until they eventually reach the surface. At the surface, these ions transfer their kinetic and potential energy to the surface in the form of increased temperature and can leave the surface as neutral species.^{20,21} It is important to stress that not all of the reactive oxygen and argon ions that approach the surface are able to interact with it, as ions can encounter other particles and undergo elastic collisions that will reflect them back to the gaseous plasma. These interactions between particles lower the probabilities of positively charged ions reaching and modifying the polymer surface.²² This is even more significant in the case of 3D samples, where the deeper layers are less exposed to the plasma than the top layers, and therefore, the probability of ions reaching them is much lower. Several authors have described a strong axial gradient of reactive oxygen radicals limiting the penetration depth of plasma and, therefore, the homogeneous surface modification on deeper layers of the sample.^{21,23} In order to address this gradient and ensure plasma treatment of the top and bottom layers of the 3D-printed mPCL samples, each scaffold was plasma-treated twice, once on each side.

A toluidine blue (TBO) assay was used to determine the surface charge and, therefore, the carboxyl group density on the surface of the modified scaffolds (Figure 2B). Importantly, longer exposure times to the plasma did not increase the surface charge when low power was used. In contrast, the use of medium and high power had a direct impact on surface charge because the COOH density increased proportionally with the exposure times. Particularly, treatment for 6 min at high power led to the highest surface charge. Regardless of the exposure time and power level used, all treated surfaces presented significantly higher carboxyl group densities than the pristine samples, which highlighted the efficiency of oxygen plasma treatment to modify the polymer surface. Plasma treatments of scaffolds at high power for 8 min or longer were not used as the temperature inside the chamber exceeded the melting point of mPCL, which led to sample degradation.

We next compared changes on the surface chemistry of plasma-treated scaffolds using XPS. Table 1 shows the elemental composition of the untreated and treated surfaces calculated from the survey spectra. For all the treated surfaces, the ratio of oxygen to carbon atoms increased in comparison with the pristine mPCL surfaces, which suggests an increase in

oxygen-containing functional groups on these surfaces. High-resolution spectra of the C 1s photoemission were acquired to identify and determine the ratios of specific carbon- and oxygen-containing functional groups present on the scaffold surface as a result of plasma treatment. Each spectrum was deconvoluted and fitted with three component peaks at binding energies of (i) 284.8 eV, corresponding to carbon-carbon and hydrogen-carbon (C-C/C-H) groups; (ii) 286.4 eV, assigned to carbon atoms singly bonded to oxygen (C-O); and (iii) 287.6 eV, attributed to O=C=O groups (SuppFigure 1). Figure 2C shows the relative concentrations of O=C=O and C-O for the control and the plasma-treated groups. In agreement with the TBO assay, all treated surfaces had a higher relative concentration of both functional groups compared with the pristine scaffolds. In particular, surfaces treated for 6 min at high power and 8 min at medium power had a significantly higher concentration of C-O bonds in comparison with the other groups.

Changes to the surface chemistry of polymers can result in undesirable effects, such as loss of mechanical properties, which play a critical role in scaffold-guided tissue engineering because scaffolds should have sufficient mechanical strength to withstand wound contraction stress and loading during not only the entire tissue regeneration process but also several remodeling cycles.²⁴ The effects of plasma treatment on the mechanical properties of mPCL were evaluated using uniaxial compression testing in PBS at a temperature of 37 °C to mimic physiological conditions. Figure 2D,E shows the strain-stress curves and the change in the elastic modulus for the treated and nontreated samples. While the elastic modulus of the scaffolds was not significantly affected by the use of low and medium power levels at all exposure times, a significant decrease of the elastic modulus was observed for the scaffolds that were exposed to high power for 4 and 6 min. Even though plasma treatment should not affect the bulk properties of materials, repetitive bond cleavage rendering ester into carboxyl groups may lead to weakening of bulk polymer chains. In addition, the use of high voltage can increase the energy that charged radicals transfer to the sample, which leads to an increase in temperature that results in polymer degradation and, therefore, loss of mechanical properties.²⁰ Particularly, the use of O₂ plasma promotes etching of the polymer surface by causing the bond cleavage and ablation of weaker polymer chains. Prolonged exposure to plasma etching can result in strong nanostructuring of the polymer surface along with a reduction in mechanical properties.²² This is congruent with other studies showing that the use of O₂ plasma for long exposure times can lead to polymer chain scission and loss of mechanical properties.^{25,26}

After characterization of the surface chemistry and mechanical properties, the scaffolds treated at high power for 6 min were selected as the most suitable surfaces for melimine immobilization because they showed the highest density of carboxyl groups among all the studied surfaces. Maximization of the density of carboxyl groups present on the surface is vital to ensure interactions with melimine because these functional groups can interact with the peptide either noncovalently, such as via hydrogen bonding and electrostatic and hydrophobic interactions, or covalently through coupling mechanisms such as carbodiimide cross-linker chemistry. Regarding the decrease in stiffness because of plasma treatment, reports from other studies^{27,28} indicate that the scaffolds still have the necessary mechanical properties to support tissue regeneration by

Table 1. Elemental Composition of % C and % O, and O/C Ratio Suggesting an Increase in Oxygen-Containing Functional Groups on Plasma-Treated Surfaces

treatment	% C	% O	O/C	
(-) control	79.5	19.8	0.25	
4 min	low	75.8	24.2	0.32
	medium	74.0	26.0	0.35
	high	75.1	24.9	0.33
6 min	low	74.2	25.8	0.35
	medium	74.5	25.5	0.34
	high	72.1	27.8	0.39
8 min	low	75.1	24.9	0.33
	medium	75.1	24.9	0.33

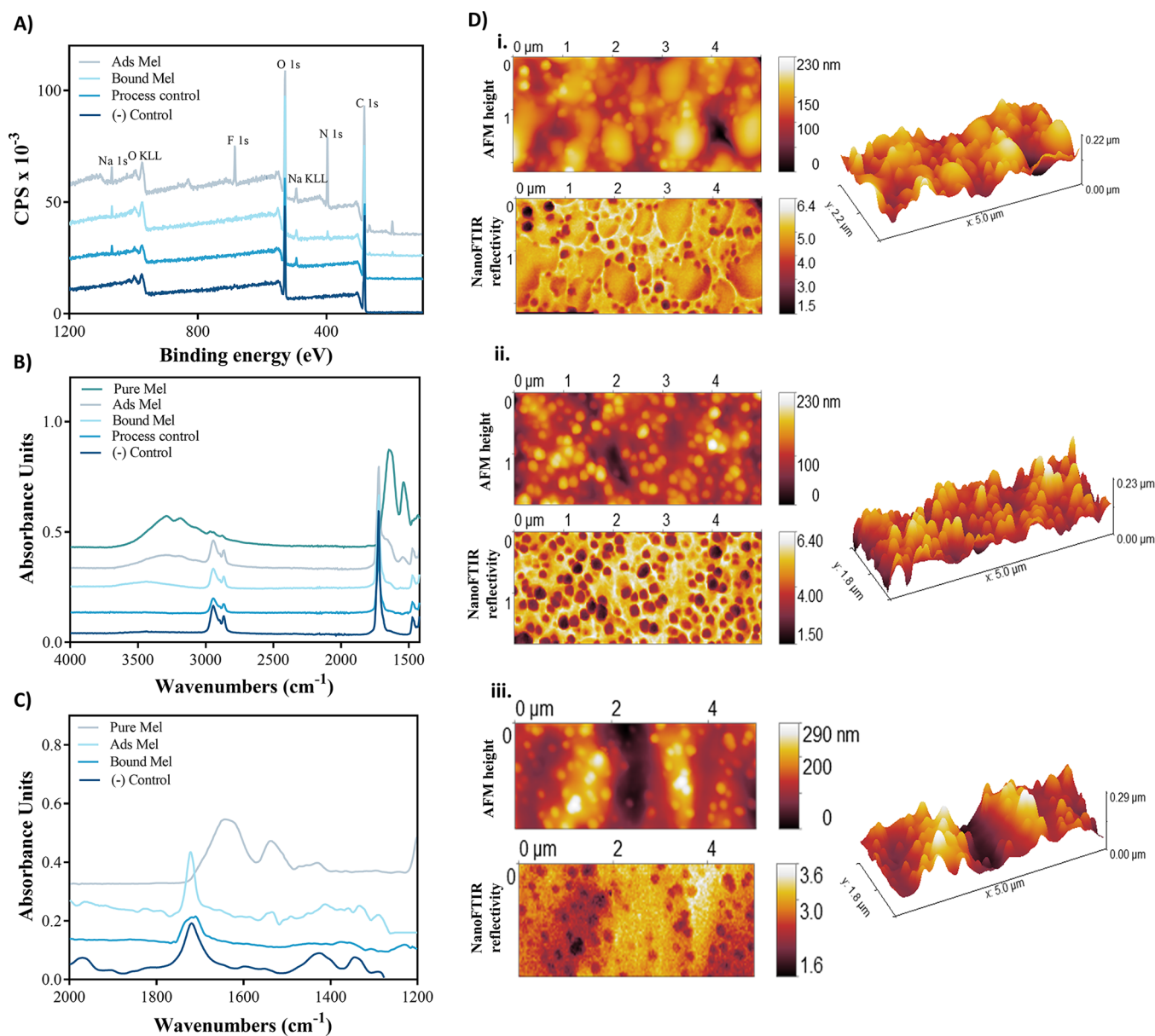


Figure 3. Characterization of the mPCL surface after melimine immobilization. (A) XPS, (B) ATR FT-IR, and (C) nanoFTIR spectra of surfaces of interest. (D) Surface nanotopography of (i) mPCL control, (ii) bound, and (iii) adsorbed melimine scaffolds.

Table 2. XPS Atomic Concentrations (atom %) of Control and Melimine-Treated mPCL Scaffolds

surface	% C	% O	% Na	% Cl	% Si	% F	% N
(-) control	78.5 ± 2.8	21.7 ± 2.8			0.05 ± 0.1		
process control	74.5 ± 1.1	24.1 ± 1.6	0.8 ± 0.5	0.6 ± 0.7			
bound melimine	70.4 ± 1.8	26.8 ± 2.8	0.5 ± 0.6				2.4 ± 0.9
adsorbed melimine	66.9 ± 2.1	22.9 ± 2.3	0.7 ± 2.0	0.7 ± 0.9		1.4 ± 2.0	7.3 ± 1.1

withstanding physiological and external loads; nevertheless, further studies need to validate this hypothesis.

2.2. Melimine Immobilization. After plasma treatment, melimine was immobilized on the mPCL surface via two different approaches: covalent binding via EDC coupling (“bound melimine”) and physical/noncovalent interactions via peptide adsorption (“adsorbed melimine”) (Figure 1). Changes on the surface chemistry and physical properties of the scaffolds due to melimine immobilization were investigated

by XPS, macro ATR FTIR, nanoFTIR, Coomassie blue staining, and contact angle measurements.

Melinime immobilization onto mPCL scaffolds was first confirmed using XPS (Figure 3A). As shown in Table 2, negative control scaffolds displayed the presence of carbon (78.5 ± 2.8% C), oxygen (21.7 ± 2.8% O) and silicon (0.05 ± 0.1% Si). By comparison, process control scaffolds showed a slight increase in the atomic concentration of oxygen (24.1 ± 1.6% O), likely because of remaining EDC intermediates bound to the surface and the presence of sodium (0.8 ± 0.5%

Na) and chloride ($0.6 \pm 0.7\%$ Cl), presumably from the buffer solution in which they were incubated. In contrast, bound and adsorbed melimine surfaces showed an increase in the atomic (%) concentration of nitrogen of $2.4 \pm 0.9\%$ and $7.3 \pm 1.1\%$, respectively, in comparison with the controls. This indicates the successful immobilization of the peptide onto the scaffold surface. Interestingly, the greater surface concentration of N for the adsorbed melimine compared with the bound melimine scaffolds suggests that more peptide interacts with the mPCL surfaces through noncovalent interactions, thereby leading to greater peptide deposition.

The results of the XPS analysis were verified by utilizing ATR FT-IR to confirm the presence of melimine on the modified surfaces (Figure 3B). The spectrum of pure melimine was first acquired to establish a reference for melimine-modified mPCL scaffolds. The spectrum of pure melimine showed vibration bands at $3200\text{--}3550\text{ cm}^{-1}$ and $1580\text{--}1650\text{ cm}^{-1}$, which corresponded to --OH and N--H functional groups. While all the untreated and treated surfaces showed the vibration of C--H and C=O peaks at $2800\text{--}3000\text{ cm}^{-1}$ and $1740\text{--}1750\text{ cm}^{-1}$ from mPCL, only the adsorbed melimine surface exhibited characteristic peaks of peptides. We hypothesize that the lack of peptide signature on the IR spectrum of bound melimine could be related to the detection limit of the technique rather than to the absence of melimine on the surface because XPS demonstrated deposition but at lower levels than for adsorption. ATR *xy* spatial resolution is $13 \times 18\ \mu\text{m}$, and the lowest concentration at which an analyte present in a matrix can be detected is $0.17\text{ wt } \%$ (1700 ppm). This limit also depends on the particle size of the analyte: if the diameter of the particles is lower than $8\text{--}15\ \mu\text{m}$, they cannot be detected by this technique.^{29,30} In light of this information, it could be possible that the concentration of bound peptide on the surface is too low to be detected by conventional FT-IR. If this is the case, we could also hypothesize that the peptide covalently binds to the surface in an organized, not agglomerated, way because the peptide particles/molecules immobilized on the surface are smaller than $8\ \mu\text{m}$.

In order to overcome the detection limits of ATR and to gain more information on the melimine-modified surfaces at nanoscale, nanoFTIR was employed. This method breaks the diffraction limit barriers and allows spectral acquisition from topographical features on the order of a few tens of nanometers by employing a near-field detection scheme. As observed in Figure 3C, nanoFTIR spectra of the control and the melimine-modified surfaces showed a common peak at $1740\text{--}1750\text{ cm}^{-1}$, which corresponded to the ester groups of mPCL. While adsorbed melimine surfaces exhibited peptide vibrations bands at $1580\text{--}1650\text{ cm}^{-1}$, bound melimine surfaces showed no peptide signal. Even though nanoFTIR should be more effective at detecting low concentrations of analyte, we hypothesize that bound melimine molecules are still too small to be detected. An additional explanation of lacking melimine signal is the prominent contribution of mPCL, which effectively masks peptide traces. The nominal spatial resolution of the nanoFTIR is approximately $10\text{--}30\text{ nm}$, depending on the probe geometry. This method has been employed in the past to detect protein-based particles larger than 12 nm ,³¹ an order of magnitude larger than the size of our individual peptide complexes. By comparison, peptides are smaller structures than proteins. For instance, melimine is a molecule of 3.8 kDa and an approximate length of $63.6\ \text{\AA}$; therefore, a group of several molecules of peptide would need to bind

together and agglomerate in order to be detected by nanoFTIR. It is interesting to note that in the case of adsorbed melimine, the peptides aggregate enough to be detected. Finally, nanotopography and optical reflectivity of modified surfaces scanned during the AFM/IF run of the nanoFTIR SNOM system (Figure 3D) revealed that all the surfaces have similar features, regardless of the way melimine was immobilized.

We furthered our understanding of the surface properties by using Coomassie blue, a dye that interacts ionically with the amino groups of peptides/proteins. As hypothesized, Coomassie blue did not stain the control and process control surfaces, as no peptide or amino-functional groups were present on those surfaces. In contrast, both melimine-modified surfaces were homogeneously stained by the dye, which suggests an even distribution of the peptide throughout the mPCL surface (SuppFigure 2Ai). As a proof of principle, Coomassie blue was detached from the surfaces and semi-quantified to provide further clues about the difference in melimine concentration on both melimine-modified surfaces (SuppFigure 2Aii). Even though there was a clear difference between the control groups and the modified surfaces, no significant difference between the adsorbed and bound melimine surfaces was found. This could be due to deviations of the Beer–Lambert law at very low concentrations, which impedes accurate establishment of a linear relationship between peptide concentration and absorbance.³² Further studies with significantly larger scaffold surface areas would be required to test this hypothesis.

Besides the characterization of the surface chemistry, changes in surface wettability as a result of melimine immobilization were also studied (SuppFigure 2B). Control and process control surfaces showed a water contact angle (WCA) of $73.3 \pm 4.6^\circ$ and $67.4 \pm 3.4^\circ$, respectively, while bound melimine and adsorbed melimine surfaces had a significantly lower WCA of $49.8 \pm 2.7^\circ$ and $38.5 \pm 4.7^\circ$, respectively. The significant increase of surface wettability when melimine is present on the surfaces is attributed to the greater presence of hydrophilic residues, such as arginine and lysine, over the hydrophobic ones in the melimine structure.³³ Interestingly, the significantly lower WCA of adsorbed melimine compared with bound melimine further confirms the evidence that adsorbed melimine surfaces have a higher density of immobilized peptide.

2.3. Peptide Distribution on the mPCL Surfaces. ToF-SIMS is a powerful technique for characterizing the composition and location of chemical species on surfaces. On the basis of a mass analysis of secondary ions (SIs) sputtered from the outer surface ($\sim 2\text{ nm}$) of a sample and with detection limits under 10 ng/cm^2 , it is capable of mapping the distribution of these ions at submicron spatial resolution.^{34,35} Herein, we use ToF-SIMS to characterize and map the distribution of melimine throughout the mPCL scaffolds surface.

Spectra were first acquired from melimine, mPCL, and melimine-modified mPCL in order to determine which ions characteristic of melimine and mPCL yield the greatest signal intensity without interfering or overlapping with signals from the other component. In the case of melimine, SI characteristics of the most abundant amino acid residues, such as arginine and lysine, are more likely to be detected at low surface concentrations of the peptide.³⁶ A full list of all the characteristic SIs of each amino acid residue comprising

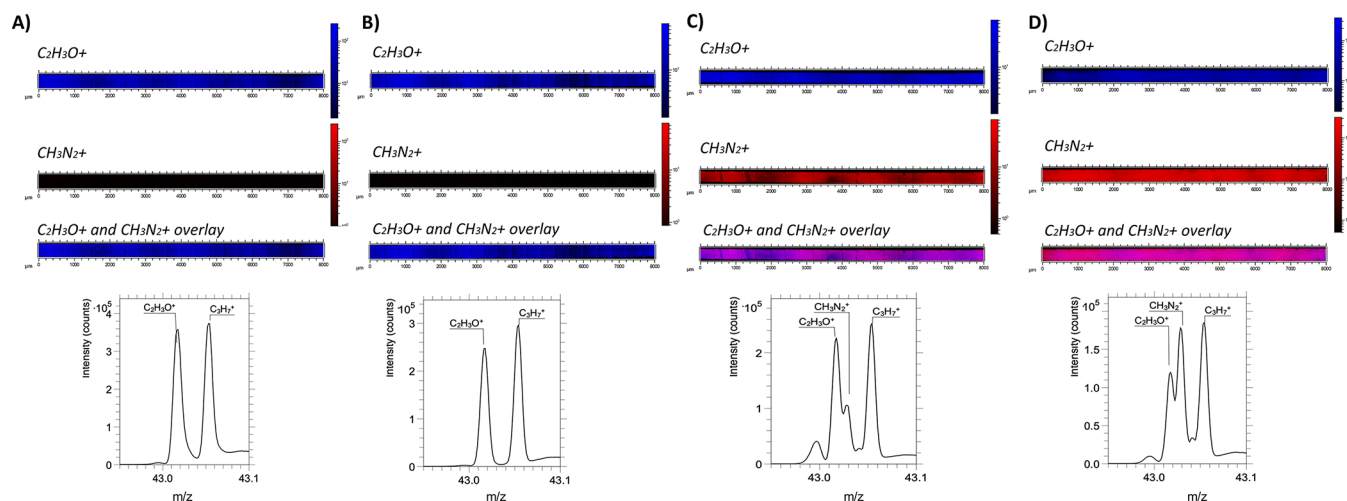


Figure 4. ToF-SIMS mapping of $C_2H_3O^+$ and $CH_3N_2^+$ ions present on (A) control, (B) process control, (C) bound melimine, and (D) adsorbed melimine surfaces. Intensity signals of $C_2H_3O^+$ and $CH_3N_2^+$ are shown in blue and red, respectively. Ion images along the struts of the scaffolds were acquired as linear sequences of $400 \times 400 \mu\text{m}$ regions, with each region rastered at $400 \times 400 \text{ px}$.

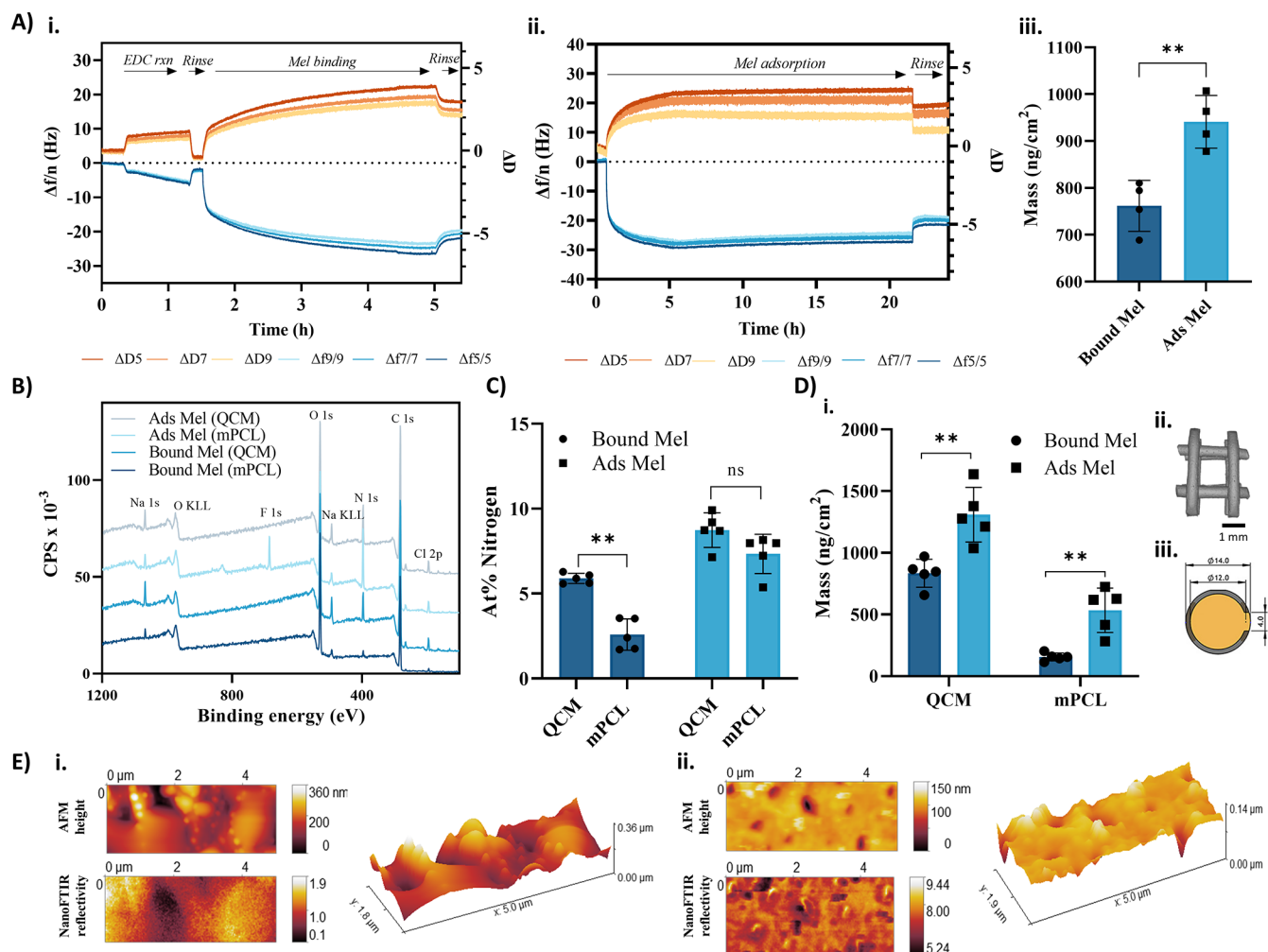


Figure 5. Quantification of melimine immobilized by covalent binding and adsorption. (A) QCM data showing the change of frequency (ΔF) and dissipation (ΔD) with the 5th, 7th, and 9th harmonics as a result of melimine (i) covalent binding and (ii) adsorption and (iii) quantification of melimine deposition on mPCL-coated QCM sensors using viscoelastic modeling. (B) XPS wide spectra of melimine immobilized on mPCL scaffolds and QCM sensors. (C) Nitrogen elemental concentration on mPCL and QCM surfaces extracted from the high-resolution XPS spectra of nitrogen. (D) Melimine mass density found on mPCL and QCM sensor surfaces by AAA. (E) Topography of mPCL scaffolds and mPCL-coated QCM sensors.

melimine is shown in [SuppTable 1](#). Even though these SIs yielded distinct peaks in the spectra acquired from pure melimine, the peaks became less distinguishable, with lower relative intensities, at the lower concentrations present on the melimine–mPCL surfaces. In addition, several SIs had masses sufficiently close to those of SIs originating from PCL to yield overlapping signals. From the results of this preliminary analysis, it was evident that the SI CH_3N_2^+ was the best candidate to detect the presence of melimine on the mPCL surface. This ion is a fragment of arginine, the most abundant amino acid in melimine, and although close in mass to the $\text{C}_2\text{H}_3\text{O}^+$ ion from mPCL, is still discernible as a distinct peak in the spectrum of melimine–mPCL.

Spectra and ion images from controls and melimine-modified scaffolds were acquired from linear sequences of $400 \times 400 \mu\text{m}$ regions along individual struts. [Figure 4](#) shows the intensities of the CH_3N_2^+ ions assigned to melimine and $\text{C}_2\text{H}_3\text{O}^+$ ions assigned to mPCL, as well as overlays of both. All the surfaces have a homogeneous distribution of $\text{C}_2\text{H}_3\text{O}^+$ ions. Interestingly, even though both melimine-modified samples showed an even distribution of CH_3N_2^+ ions across each strut, there was a clear increase in the relative intensity of CH_3N_2^+ on the adsorbed melimine sample. This observation is consistent with XPS and other surface characterization data showing that when melimine is adsorbed onto the surface there is a greater peptide concentration than when melimine is immobilized by covalent bonding.

Even though ToF-SIMS is not as widely used for the surface characterization of polymers as other techniques, such as XPS and ATR FT-IR, there are a few studies employing this technique for the study of functionalized PCL surfaces, such as PCL-spin-coated glass slides,³⁷ PCL films cast on glass,³⁸ and electrospun mats.³⁹ To the best of our knowledge, ToF-SIMS has not been previously used to characterize 3D-printed mPCL scaffolds that have been functionalized with peptides.

2.4. Melimine Quantification. After detailed surface characterization of the melimine-modified mPCL scaffolds, the mass of peptide immobilized by covalent binding as well as by adsorption was quantified by quartz crystal microbalance with dissipation monitoring (QCM-D) and amino acid analysis (AAA). In the case of QCM-D, melimine was immobilized onto gold QCM sensors spin-coated with mPCL. The change in frequency (ΔF) and dissipation (ΔD) were simultaneously measured to gain information about mass change and the viscoelastic properties throughout each step in the process of melimine immobilization. Perhaps of greater interest, a decrease in frequency is related to an increase in peptide binding, while an increase in frequency accounts for a loss of mass deposited on the sensor. In contrast, the dissipation is dependent on the viscoelastic properties of the deposited layer, a decrease in dissipation suggests stiffening of the deposited layer, while an increase in dissipation is related with softer structures.⁴⁰

QCM data collected during the immobilization of melimine on mPCL-coated QCM sensors are shown in [Figure 5A](#). During covalent immobilization of melimine on the QCM sensors ([Figure 5Ai](#)), the variations in frequency and dissipation provided evidence of the changes in mass at each step of the peptide coupling. For instance, an initial continuous decrease of frequency was observed during the EDC reaction, thereby showing that EDC molecules bind to the sensor surface. After 45 min, the reaction was stopped, and buffer was flow for 10 min into the QCM chamber, which led to an

increase in frequency as unbound EDC molecules were washed off from the surface. Once melimine was injected into the system, the frequency decreased rapidly during the first hour and then approached stability toward the end of the reaction. The sensor was then washed with buffer in order to remove unbound melimine. In the case of adsorbed melimine on the QCM sensors ([Figure 5Aii](#)), there was a rapid decrease of frequency when the sensor was exposed to melimine. After almost 5 h, the frequency shift stabilized, presumably because the surface was saturated with the peptide. The surface was then washed, which led to an increase in frequency because of the removal of unbound melimine. Viscoelastic modeling tools were used to calculate the density of immobilized peptide. The calculated density of melimine on the covalently bound surfaces was $761.7 \pm 54.2 \text{ ng/cm}^2$, while the density on the surfaces where melimine was adsorbed was $941.1 \pm 56.1 \text{ ng/cm}^2$ ([Figure 5Aiii](#)). These data are congruent with the surface characterization results that show adsorbed melimine surfaces to have a higher concentration of peptide than bound melimine scaffolds.

Even though the mass of melimine immobilized onto the mPCL-spin-coated sensors was calculated, it is unknown whether this information can be extrapolated to the 3D-printed scaffolds used for this study. In order to investigate the accuracy of this comparison, XPS survey spectra ([Figure 5B](#)) and high-resolution N 1s spectra ([Figure 5C](#)) for melimine bound and adsorbed onto mPCL scaffolds and mPCL-coated QCM sensors were compared. Interestingly, bound melimine on QCM sensors showed significantly higher elemental nitrogen in comparison to the mPCL scaffolds, which suggested that more melimine was covalently bound onto the sensor. In the case of melimine adsorption, QCM sensors showed a higher nitrogen content than mPCL scaffolds; however, this difference was not significant. We hypothesize that these variations could be due to the differences in which both surfaces were exposed to melimine. For instance, when mPCL scaffolds were used, each scaffold was placed in an independent well in the well plate, and a defined volume of melimine solution was added. This solution remained in the well throughout the reaction time. In the case of QCM sensors, fresh melimine solution was pumped into the QCM chamber during the reaction time. In principle, the continuous pumping of melimine contributes to more peptide interacting with the surface because more fresh solution is used during the reaction. In addition, the constant flow could also play a role in increasing the physical interactions between the surface and the peptide.

Because of the variations in the elemental nitrogen relative concentration on QCM and mPCL scaffolds revealed by XPS, AAA was used to quantify the amount of peptide covalently bound and adsorbed on both surfaces. [Figure 5D](#) shows the mass density for all the surfaces, mPCL bound and adsorbed melimine showed a mass density of 155.5 ± 31.7 and $533.5 \pm 179.9 \text{ ng/cm}^2$, respectively, while QCM bound and adsorbed melimine had a mass density of 834.5 ± 113.1 and $1308.9 \pm 221.6 \text{ ng/cm}^2$, respectively. This result confirmed that more peptide was immobilized on QCM sensors either by covalently binding or adsorption. Adsorption of melimine on both mPCL and QCM sensors' surfaces led to the greatest peptide concentrations, which suggests that melimine interacts strongly with mPCL by noncovalent interactions.

In this study, a broad variety of surface characterization techniques have been used in conjunction in order to enrich

the understanding of the surface properties of a clinically widely applied biodegradable polymer, namely mPCL. For instance, ATR-FTIR and nanoFTIR provided insights on the availability and conformation of melimine on the surface, while XPS offered a semiquantitative analysis of the peptide concentration on the scaffolds. In contrast, ToF-SIMS offered a detailed characterization of the peptide distribution on the surfaces. Finally, QCM-D and AAA provided a precise quantification of melimine density on QCM and mPCL scaffolds. Altogether, with their different resolutions and limitations, these techniques complemented each other and helped gain deeper understanding of the changes in the mPCL surface due to melimine immobilization. Table 3 provides a summary of the techniques used in this study and highlights their advantages and limitations. In addition, the number of publications in which these techniques were used for surface characterization of materials in the last 10 years was added in order to stress how widely or narrowly these techniques are used.

2.5. Intramolecular Interactions between mPCL and Melimine. A computational study using molecular docking was carried out in order to better understand and identify noncovalent interactions between mPCL and melimine. First, the three-dimensional structure of melimine was predicted de novo. As shown in Figure 6B, melimine contains an α helix from the amino acid residues Thr-1 to Lys-11, and the rest of the residues extend linearly. This type of secondary structure could provide the electrostatic potential on the surface to form short-range interactions, like salt-bridges and hydrogen bonds, with mPCL.

Once the melimine structure was built, a set of 30 mPCL ligands based on a combination of caprolactone (A) and its protonated state resulting from plasma treatment (B) were constructed and docked on its surface. Each ligand generated nine docked poses, and each pose was used to calculate noncovalent interactions with melimine. This analysis pointed out three main types of noncovalent interactions: hydrophobic, hydrogen bonding, and salt bridge, the latter involving hydrogen bonds and electrostatic interactions. As shown in Figure 6C, hydrophobic and salt bridges are the most common interactions, presumably because of the long hydrophobic alkane chain of caprolactone and the affinity of the carbonyl and hydroxyl groups to interact with lysine and arginine residues of melimine. As an illustration, Lys-7 and Arg-10 are the amino acid residues with the highest frequency of interactions.

To obtain a better understanding about how these interactions are caused, all the different interactions established by each ligand and melimine are presented in Figure 6D. In general, larger ligands had more interactions than smaller ligands. However, some cases are worth mentioning, such as the dimer BA and BAAA. The first one has eight hydrophobic interactions, three salt bridges and one hydrogen bond. Conversely, BAAA has only two hydrophobic interactions and one salt bridge. In addition, structures had more interactions when B was present. This comparison indicates that protonation, which is achieved experimentally by plasma-treating the mPCL scaffold, directly influenced the number of interactions involved in the binding.

We identified the differences in binding of deprotonated and protonated structures by comparing the 3D representation of a tetramer with only deprotonated structures (AAAA) that only had 10 interactions with melimine and the tetramers with ≥ 14

Table 3. Review of Surface Characterization Techniques Used in This Study Highlighting Their Resolution, Advantages and Limitations^{30,31,34,35,41}

surface characterization technique	detection functional groups	detection limit	advantages	limitations	key references	# of publications (2012–2022)
ATR-FTIR	functional groups	8–15 μm 0.17%, 1700 ppm	simple, quick and accessible	sample is often damaged when pressing against the diamond crystal	Lanzarotta, 2015 ³⁰	2241
nanoFTIR	functional groups	10–30 nm	simultaneous IR spectra and AFM data acquisition providing information on the presence and location of specific functional groups	not suitable for molecules smaller than proteins such as peptides	Amenabar et al., 2013 ³¹	20
XPS	elements	0.1–1 At % 1 μm	provides qualitative and quantitative information about the chemical composition of a material	lack of molecular specificity	Shard, 2014 ⁴¹	610
ToF-SIMS	ions	~ 2 nm 10 ng/cm ²	allows precise characterization of the chemical composition and distribution of an analyte on the surface	quality of data is strongly dependent on the topography of the surface, features of the order of microns can lead to lateral distortion and shadowing of the image	Taylor et al., 2018 ³⁴	45
QCM-D	mass	~ 1 ng/cm ²	allows to monitor real-time changes in the surface deposited mass and viscoelastic properties	molecules need to be immobilized and quantified on quartz crystal which might not resemble the real sample surface	Baio et al., 2020 ³⁵	76

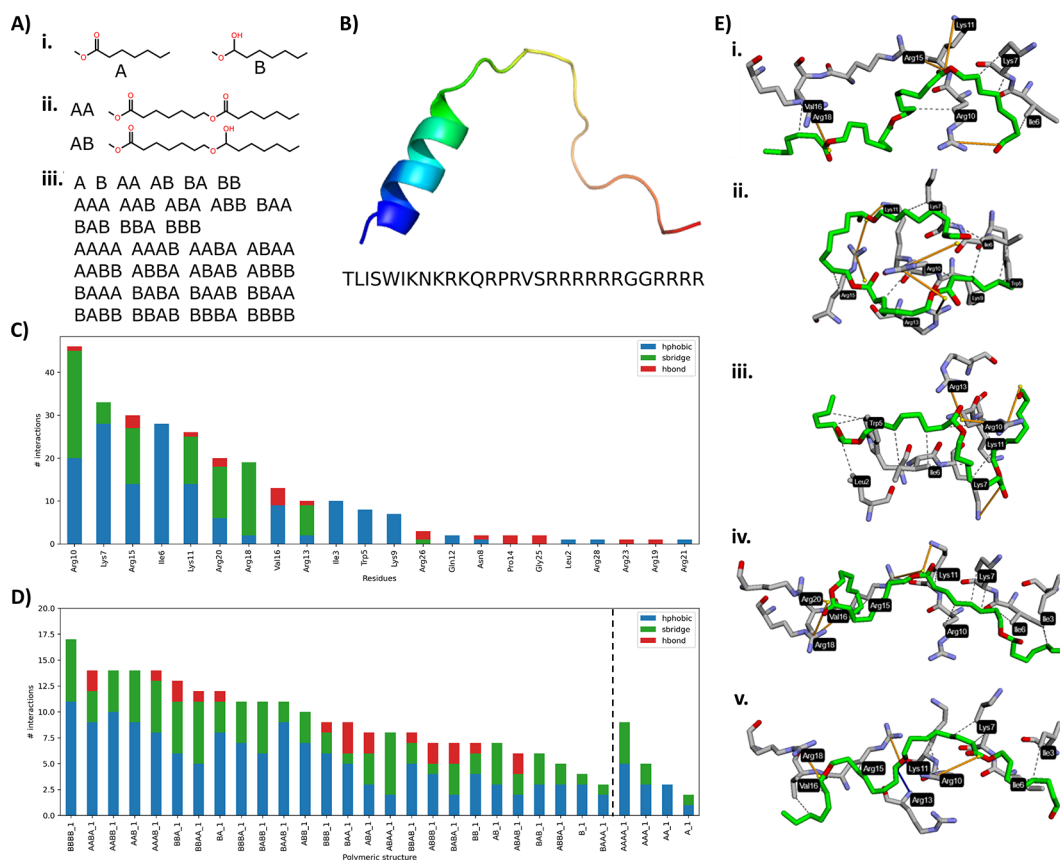


Figure 6. (A) Set of ligands docked with melimine: (i) structures of caprolactone deprotonated and protonated, (ii) construction of ligands using different patterns, and (iii) set of combinations used in ligand generation. (B) Structure and sequence of melimine. (C) Frequency of noncovalent interactions with melimine including only the best pose of each ligand. (D) Number and interaction types of each ligand. (E) 3D representation of the binding mechanism with melimine: (i) AAAAA, (ii) BBBBB, (iii) AAAB, (iv) AABB, and (v) AABA. Salt bridges are illustrated in orange solid lines, hydrophobic interactions are in dashed gray lines, and hydrogen bonds are in solid blue lines.

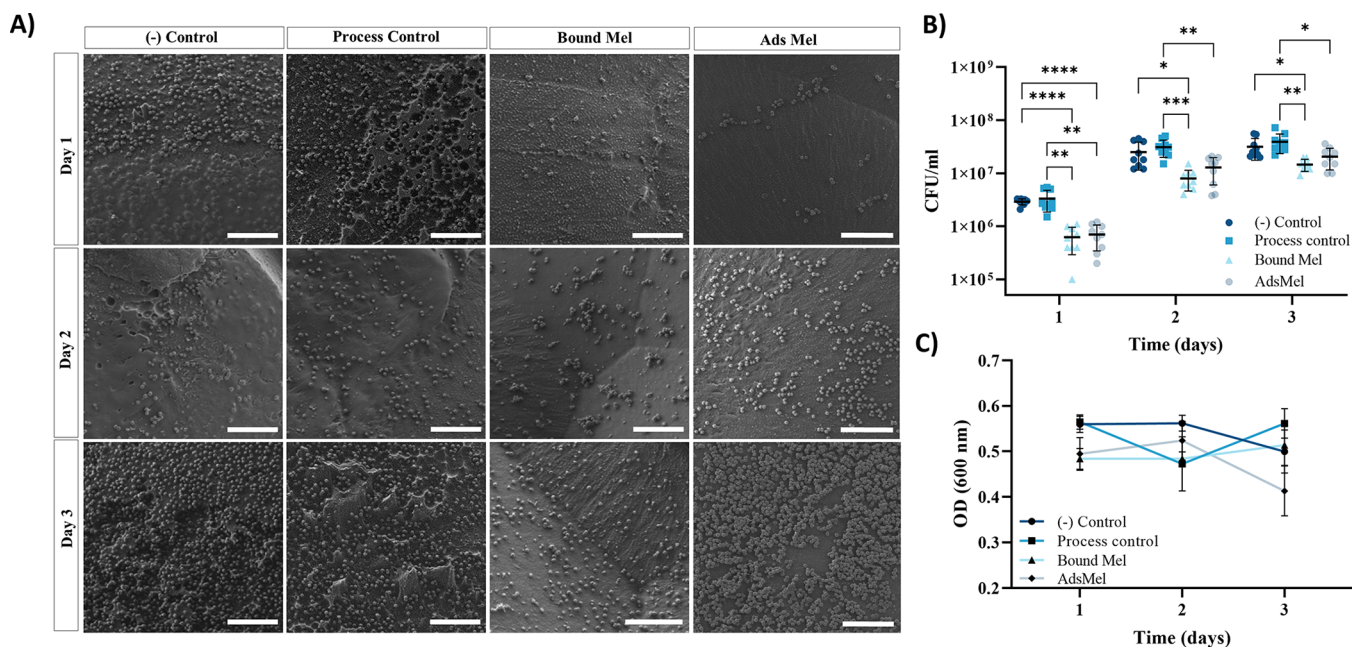


Figure 7. *In vitro* evaluation of melimine-modified scaffolds' antimicrobial properties against *S. aureus* for 3 days. (A) SEM images evidencing extensive bacterial colonization on the control and process control surfaces in comparison with both melimine-modified scaffolds. (B) Number of viable colony forming units of bacteria recovered from each scaffold at each day. (C) OD measurement of the media in which scaffolds were incubated. Data shown as mean \pm SD; * $p < 0.05$, ** $p < 0.01$, *** $p < 0.001$, **** $p < 0.0001$ ($n = 9$); scale bars, 10 μm .

interactions (BBBB, AABB, AAAB, AABA), 17 in the case of BBBB and 14 for the others (Figure 6E). These diagrams indicate that several interactions were present in all the structures, such as hydrophobic interactions with Ile6, Lys7, and Arg10 and salt bridges with Lys11 and Arg10. Interestingly, these tetrameric structures tended to twist around Arg10, which indicates that this amino acid residue could be a key residue involved in the binding of mPCL. Moreover, structures with at least one protonated structure (B) seemed to wrap closer to Arg10 and form salt bridges with two carboxyl groups. In conclusion, this analysis highlights the importance of lysine and arginine residues in the formation of noncovalent interactions with mPCL. More importantly, it showed that long chains of mPCL could bind around the α helix to form a strong interaction on the basis of several salt bridges.

2.6. *In vitro* S. aureus Adhesion on Melimine-Modified Scaffolds. The antibacterial efficacy of melimine-modified surfaces was assessed *in vitro* by exposing the scaffolds to *S. aureus* for 24 h and incubating them for 3 days in LB media to allow bacterial growth and biofilm formation. Bacterial colonization and biofilm formation on the unmodified and modified surfaces was followed by SEM imaging, cfu counting, and OD measurements over 3 days. Figure 7A shows the SEM images of bacterial colonization on all the surfaces at each time point. After the first day, there was significant bacterial colonization on the control scaffolds, as well as initial formation of biofilm. In contrast, both bound and adsorbed melimine surfaces had significantly less adhered bacteria. Bound melimine had a decrease in bacterial colonization of $78.7 \pm 11.3\%$ and $81.3 \pm 9.9\%$ in comparison with the control and the process control, respectively. Adsorbed melimine had $76.0 \pm 12.2\%$ and $78.9 \pm 10.7\%$ fewer bacteria than the control and process control, respectively, which verifies the antimicrobial properties of the mPCL scaffolds when melimine is immobilized onto the surface. After 2 and 3 days, both control scaffolds demonstrated an increase in bacteria numbers and the formation of biofilms. By comparison, even though more bacteria adhered to the melimine-modified scaffolds during this time, there was still no evidence of biofilm formation. Importantly, the prevention of biofilm formation during the first days after implantation is essential to ensure integration of the implant.

Although not significant, adsorbed melimine surfaces had a slightly lower reduction in *S. aureus* colonization in comparison with the bound melimine surfaces, especially after 3 days of incubation (Table 4). This could be due to the release of melimine as noncovalent interactions may not be strong enough to maintain the peptide immobilized on the surface. As

Table 4. Reduction in *S. aureus* Colonization on Melimine-Treated Surfaces in Comparison with the Control and Process Control Surfaces

reduction in <i>S. aureus</i> colonization (%)	day 1	day 2	day 3
bound melimine – control	78.7 ± 11.3	68.0 ± 13.5	53.9 ± 11.9
bound melimine – process control	81.3 ± 9.9	74.3 ± 10.9	63.0 ± 9.5
adsorbed melimine – control	76.0 ± 12.2	48.4 ± 27.5	34.8 ± 28.4
adsorbed melimine – process control	78.9 ± 10.7	58.6 ± 22.1	47.7 ± 22.8

a proof of principle, the adsorbed melimine-modified scaffolds were incubated in PBS for 3 days, and XPS spectra of the scaffolds' surfaces were acquired at each day, with the hypothesis that a release of melimine from the surface will result in a decrease in the relative concentration of elemental nitrogen. As observed in SuppFigure 7, bound melimine surfaces did not experience significant changes in atom % nitrogen, which suggests no loss of melimine. In contrast, the elemental concentration of nitrogen on adsorbed melimine surfaces decreased from $7.3 \pm 0.9\%$ to $3.6 \pm 1.0\%$ after only 1 day of incubation, thereby suggesting a release of melimine from the surfaces. Interestingly, the nitrogen elemental concentration of bound and adsorbed melimine surfaces after 3 days was similar at $2.5 \pm 0.4\%$ and $2.8 \pm 0.5\%$, respectively. This suggests that the lower antimicrobial efficacy of adsorbed melimine surfaces is dependent on the type of interactions with the mPCL surface. Release kinetics and peptide stability studies will be the focus of our future research.

Previous studies have demonstrated greater antibacterial activity of melimine when covalently bound to surfaces in comparison with adsorption. For instance, adsorption of 500 μg of melimine to Etalicon A hydroxyethyl methacrylate contact lenses resulted in a reduction of bacterial colonization by 80%; in comparison, when melimine was covalently bound on the same surfaces, 18 μg of peptide were immobilized, and this resulted in bacteria adhesion reduction of 70%. The significantly lower concentration of melimine needed when covalent binding was used to give an almost similar level of activity suggests that there is greater surface availability of covalently bound compared with adsorbed melimine where the peptide aggregates and leaches from the surface.¹⁰ Some studies support this hypothesis because covalent immobilization of AMPs onto different biomaterial surfaces increased their long-term stability *in vivo* as it confers protection against enzymatic degradation and aggregation.^{42,43}

Melimine has also shown to successfully reduce bacteria adhesion and biofilm formation when covalently bound to different nondegradable materials such as silicone, glass, and titanium.^{10,11,33,44} For instance, significant antimicrobial activity against *Acanthamoeba*, fungi, and antibiotic-resistant *Pseudomonas aeruginosa* and *S. aureus* was produced by immobilizing melimine onto the surface of hydroxyethyl methacrylate contact lenses by EDC covalent coupling.¹¹ In previous studies, melimine was tethered to an amine-functionalized titanium surface via a thioether linkage between the cysteine at the melimine N-terminus and the maleimide moiety at the functionalized titanium surface. The resulting melimine-treated surface produced a significant decrease in *in vitro* bacteria attachment and biofilm formation of *P. aeruginosa* by up to 62% and *S. aureus* by up to 84% on the treated surface in comparison with the untreated control. Additionally, the melimine-coated titanium surface successfully reduced bacteria colonization by up to 2 \log_{10} compared with the uncoated surface over 5–7 days in mouse and rat subcutaneous infection models without showing any cytotoxic effect at active concentrations.⁴⁵

3. CONCLUSIONS

This study characterized the surface chemistry and mechanical properties of mPCL scaffolds when exposed to different conditions of plasma treatment and after immobilization of melimine, an antimicrobial peptide that has been tested in

Phase I and II human clinical trials, by covalent bonding or adsorption.

Detailed surface characterization of melimine-modified surfaces demonstrated the presence of the peptide, as well as its homogeneous distribution throughout the scaffold's surface. Melimine covalent binding resulted in a peptide density of ~ 156 ng/cm² and led to a reduction of *S. aureus* colonization by 78.7%. In contrast, melimine adsorbed to mPCL resulted in higher peptide density of ~ 533 ng/cm² but a slightly lower bacterial colonization reduction of 76.0%. These results suggest a higher antimicrobial activity of melimine when covalently bound to surfaces, presumably because of higher surface availability and proper peptide orientation that might not be achieved when the peptide aggregates on the surface as part of the adsorption process.

In conclusion, the results of this study showed the *in vitro* efficacy of the melimine-treated mPCL surfaces against bacterial colonization and biofilm formation.

4. METHODS AND EXPERIMENTAL

4.1. Materials. Melimine (TLIS-WIKNKRKQPRVSRRRRRRGGRRRR) was purchased from the Auspep Peptide Company (Australia) at a purity equal or higher than 90%. Purasorb medical grade polycaprolactone (MW: 50 000 Da) was acquired from Corbion (Netherlands). Gram-positive *Staphylococcus aureus* (*S. aureus* ATCC 29213) was procured from In Vitro Technologies (Victoria, Australia). QCM 5 MHz 14 mm Cr/Au sensors were obtained from QuartzPro (Sweden). Luria–Bertani (LB) broth and agar were acquired from Thermo Fisher Scientific (USA). All chemicals were purchased from Merck (Germany) unless specified otherwise.

4.2. Methods. **4.2.1. Scaffold Fabrication.** Lattice scaffolds of 50 × 50 × 2 mm in size and macropores of 1 × 1 mm were 3D-printed using a BioScaffolder 3.1 (GeSiM mbH, Germany) at a printing temperature of 80 °C. Scaffolds were cut into smaller pieces of 4 × 4 mm and these were used for all surface modification/characterization studies.

4.2.2. Plasma Treatment. The surface of mPCL scaffolds were treated using a vacuum plasma cleaner (PDC-002-HP Harrick Plasma, USA) under O₂/Ar₂ for 4 and 6 min at low (30W), medium (38W), and high (45W) power, and for 8 min at low and medium power. Each scaffold was plasma-treated twice, once on each side (top and bottom).

4.2.3. Toluidine Blue O Staining. The presence of carboxylic groups on the mPCL surface, as a result of plasma treatment, was determined using toluidine blue O (TBO) staining.⁴⁶ Scaffolds were incubated in 0.5 mM TBO pH 10.0 for 5 h at room temperature and under gentle shaking. Samples were then rinsed multiple times with 0.1 mM NaOH, pH 10.0, until the unbound dye was fully removed. Samples were incubated in 50% acetic acid under gentle shaking for 10 min to enable unbinding of the dye. Solutions were transferred to a 96-well plate in triplicate, and the absorbance was read at 633 nm. In addition, a standard curve of known TBO concentrations was prepared in 50% acetic acid. The density of carboxylic groups (nmol/cm²) was calculated assuming a 1:1 mol binding efficiency between TBO and carboxyl groups.

4.2.4. X-ray Photoelectron Spectroscopy (XPS). Surface chemical characterization of pristine, plasma-treated, and melimine-modified scaffolds was performed via XPS (AXIS Ultra, Kratos Analytical, UK). Survey spectra and high-resolution C 1s, O 1s, and N 1s spectra were recorded at three random locations on each scaffold at a pass energy of 150 and 40 eV, respectively. The pressure inside the analysis chamber was maintained below 1×10^{-8} Torr during the data acquisition. Atomic concentrations of the elements present on the surface were calculated from the survey spectra using the CasaXPS software. Additionally, CasaXPS was used to deconvolute the high-resolution C 1s spectra into contributions from three peaks, with

binding energies of 284.8 eV corresponding to carbon–carbon and hydrogen–carbon bonds (C–C/C–H), 286.4 eV assigned to carbon singly bonded to oxygen (C–O), and 287.6 eV associated with O–C=O bonds. Peak fitting was performed using a U2 Tougaard background and a Gaussian/Lorentzian [GL(30)] line shape for the component peaks.

4.2.5. Mechanical Testing. Mechanical properties of pristine and plasma-treated scaffolds were assessed by uniaxial compression testing using an Instron model 5848 (Melbourne, Australia) with a 500N load cell. Testing was performed at a compression rate of 0.1 mm/s, in phosphate buffer saline (PBS) at a temperature of 37 °C to mimic physiological conditions. Elastic modulus (MPa) was calculated by the gradient of the stress–strain curve over the region of linear elastic behavior (0–10% strain).

4.2.6. Melimine Immobilization. Plasma-treated scaffolds were sterilized by exposure to 70% v/v ethanol followed by evaporation. Melimine was immobilized onto the surface by covalent bonding and by adsorption. For the covalent attachment of melimine, scaffolds were incubated in 2 mg/mL of 1-ethyl-3-(3-dimethylaminopropyl) carbodiimide hydrochloride (EDC) in acetate buffer for 45 min at room temperature under gentle shaking. After EDC binding to the mPCL surface, the scaffolds were washed twice with PBS pH 7.4 and subsequently incubated with a solution of 2 mg/mL of melimine in PBS for 5 h to allow covalent binding. Then, the scaffolds were rinsed several times with PBS to remove unbound peptide. Immobilization of melimine by adsorption was performed by incubating sterile scaffolds in a 2 mg/mL solution of melimine in PBS for 5 h under gentle shaking. After shaking, the scaffolds were washed twice with PBS to remove excess unbound peptide (Figure 1).

4.2.7. Attenuated Total Reflection Fourier Transform Infrared Spectroscopy (ATR FTIR). ATR FTIR spectra of unmodified and melimine-treated scaffolds, as well as pure melimine, were acquired using a Bruker Alpha-P spectrometer (Bruker, USA) with a diamond crystal ATR. IR absorbance spectra were collected in the wavenumber region of 400–4000 cm⁻¹ at a spectral resolution of 1 cm⁻¹.

4.2.8. Nanoscale Fourier Transform Infrared Spectroscopy (nano-FTIR). A scattering type scanning near-field optical microscope (s-SNOM) nanoFTIR was employed on a NeasNOM (neaspes GmbH, Germany) platform equipped with PtIr-coated atomic force microscopy (AFM) Si probes (neaspes GmbH, Germany) of 260 kHz nominal resonance frequency and nominal contact radius better than 25 nm. Topography data was acquired by employing amplitude modulation AFM tapping mode and optical amplitudes and single-point IR absorbance spectra were recorded using a broadband mid-infrared laser (600 to 2100 cm⁻¹) focused onto the metallized AFM tip. More details about the method can be found in Huth et al.⁴⁷ Typical data acquisition parameters are 80 nm free tapping amplitude and 80% set-point, 10–20 ms integration times, and at least three averages/point for each spectrum. Spectral data was processed (phase tilt and offset adjusted) utilizing neaPLOT (ver. 1.9.719) software.

4.2.9. Coomassie Blue Staining. Scaffolds were stained with coomassie blue, a dye that interacts ionically with amino groups of peptides/proteins, to investigate the distribution of immobilized peptide on the surfaces.¹⁰ Controls and bound and adsorbed melimine surfaces were stained for 6 h with filtered 0.025% coomassie blue in 10% acetic acid and 10% isopropanol at 37 °C under gentle shaking conditions. The scaffolds were then washed twice and incubated for 1 hour with a solution of 10% acetic acid and 10% isopropanol to remove unbound dye. Finally, scaffolds were incubated in 50% acetic acid for 10 min under gentle shaking to enable the unbinding of coomassie blue. The solutions were transferred to a 96-well plate in triplicate, and the absorbance was read at 600 nm.

4.2.10. Water Contact Angle (WCA). The contact angles of unmodified and modified scaffolds were measured using the Biolin ThetaFlex drop shape (Biolin Scientific, Sweden). Briefly, a 2 μ L droplet of water was deposited on flat mPCL scaffolds, and the contact angle was imaged and quantified using the software OneAttention.

4.2.11. Time-of-Flight Secondary-Ion Mass Spectrometry (ToF-SIMS). The mPCL scaffolds analyzed by ToF-SIMS comprised four

layers of PCL struts and were cut to $1 \times 1 \text{ cm}^2$. Each scaffold was secured to the sample holder with silver paint and oriented so that the bottom layer (i.e., the one printed first) was uppermost. The bars of this layer were flattened by contact with the glass substrate during printing, thereby creating surfaces more suitable for ToF-SIMS analysis than the cylindrical surfaces of the bars in subsequent layers. Data were acquired using an IONTOF M6 instrument (IONTOF GmbH, Germany) equipped with a reflectron time-of-flight analyzer and 30 kV Bi/Mn primary-ion source. Bi_3^+ cluster ions were selected from the pulsed primary-ion beam for the analysis and were “unbunched” to attain submicron spatial resolution. In order to also attain the mass resolution necessary to differentiate signals from the melimine coating and those from the PCL, the analyzer was operated in delayed-extraction mode ($m/\Delta m > 5000$).⁴⁸ A cycle time of 75 μs provided an accessible mass range up to 500 u.

Ion images along the bars of the scaffolds were acquired as linear sequences of $400 \times 400 \mu\text{m}$ regions, with each region raster-scanned at 400×400 pixels. The primary-ion dose for each image was 2.5×10^{11} ions cm^{-2} . Surface charging was compensated for by flooding the samples with low-energy (21 eV) electrons between primary-ion pulses. The data were acquired in positive polarity, and the mass scale was calibrated using peaks attributed to hydrocarbon ions (C_2H_3^+ , C_2H_5^+ , and $\text{C}_{3-7}\text{H}_7^+$). The pressure in the analysis chamber was at, or below, 5×10^{-9} mbar.

4.2.12. Quartz Crystal Microbalance with Dissipation (QCM-D). Covalent binding and adsorption of melimine on mPCL spin-coated QCM sensors was quantified using a Q-sense system (Biolin Scientific, Sweden). Briefly, 14 mm Cr/Au QCM sensors with a fundamental frequency of 5 MHz were spin-coated with a 2% mPCL w/v solution in chloroform for 30 s at 3500 rpm. Coated sensors were then plasma-treated for 6 min at high power and subsequently used for either melimine covalent binding or melimine adsorption. In both cases, coated sensors were placed in the QCM chamber, and the change in frequency (ΔF) and dissipation (ΔD) with the fifth, seventh, and ninth harmonics were recorded. Initially, buffer solution was pumped into the chamber at a flow rate of 50 $\mu\text{L}/\text{min}$ until a stable baseline was achieved. Once the signal was stabilized, melimine binding and adsorption were performed. In the case of covalent binding, EDC solution was passed into the system for 45 min, then PBS was pumped for 15 min in order to rinse the sensor surface. Finally, melimine solution was injected to allow covalent binding; at the end of the reaction, buffer was pumped again to remove unbound peptide. In the case of melimine adsorption, melimine was injected into the system at a flow rate of 50 $\mu\text{L}/\text{min}$ for 20 h to establish the time it takes for the surface to be saturated with melimine. Collected data were analyzed using the software QSense Dfind, and the mass density of immobilized melimine was quantified using viscoelastic modeling.

4.2.13. Amino Acid Analysis (AAA). Melimine immobilized onto mPCL scaffolds and QCM sensors by covalent binding or adsorption was quantified using highly sensitive amino acid analysis (gas phase hydrolysis). QCM sensors were broken into small fragments to fit into the vials used for the hydrolysis. Sensors fragments as well as scaffolds were transferred into hydrolysis vials and underwent 24 h gas phase hydrolysis in 6 M hydrochloric acid at 110 °C. After hydrolysis, the samples were dried, then reconstituted in 0.5 mL 0.05% TFA/Milli-Q water, mixed, and allowed to stand for 1 hour at room temperature before mixing again. Aliquots of 450 μL were then dried for analysis. All amino acids were labeled, with the inclusion of an internal standard using the Waters AccQTag Ultra chemistry and analyzed on a Waters Acquity UPLC. At these conditions, asparagine was hydrolyzed to aspartic acid, and glutamine was hydrolyzed to glutamic acid; hence, the reported amount of aspartic and glutamic acid is the sum of those respective components.

4.2.14. In Silico Melimine–mPCL Interaction Profiling. The three-dimensional structure of melimine was predicted *de novo* using the PEP-FOLD 3.5 server.⁴⁹ A set of 30 ligands of different sizes (from 1 to 4 monomeric units) based on a combination of caprolactone (A) and its protonated state (B) was constructed with ACD/ChemSketch,

version 2021.2.0. The structures of A and B and the ligands are summarized in Figure 6A.

Molecular docking of these ligands with melimine was carried out with GNINA 1.0.⁵⁰ This step generated nine docked poses for each ligand. These poses are ranked on the basis of a score that indicates how close the pose is to a perfect conformation. Nevertheless, the size and flexibility of the ligands involved in this study should not be considered as a prediction, but accompanied with expert knowledge and available experimental data that might offer an insight of what are the most relevant characteristics involved in melimine attachment to PCL. For this reason, noncovalent interactions of melimine with each docked pose were calculated using PLIP.⁵¹

4.2.15. 3D Broth Assay. Treated and untreated scaffolds were incubated in 0.5 mL of *S. aureus* (ATCC 29213) suspension at a concentration of 1×10^8 colony forming units (cfu)/mL at 37 °C for 3 days. At each time point (day 1, 2, and 3), scaffolds were separated for analysis while the others were used to continue the experiment until day 3. In the case of analysis, scaffolds with adherent bacteria were transferred to another well plate, washed three times with PBS to remove unadhered bacteria, and then used for cfu counting and SEM imaging. The remaining scaffolds used to continue the experiment were placed in another well plate, and fresh LB media was added at each time point.

4.2.15.1. CFU Counting. Scaffolds were placed in 1.5 mL low-binding Eppendorf tubes with 1 mL of PBS. Bacteria adhered to the scaffold surfaces were detached by two 15 min cycles of sonication at 100 rpm with a 10 s vortexing step before and after sonication. The resulting bacteria suspensions were serially diluted in PBS, and 5 μL aliquots of each suspension were plated onto LB agar and incubated overnight at 37 °C. After incubation, the cfu were counted.

4.2.15.2. SEM Imaging. Scaffolds were fixed for 3 h with 2.5% w/v glutaraldehyde and then washed three times with PBS. The samples were then dehydrated via a series of ethanol treatments with increasing concentrations from 10% to ~100% v/v by using a Pelco BioWave Microwave Tissue processor. Once dehydrated, the scaffolds were coated with a 5 nm layer of platinum via a Leica EM-SCD005 cool sputter coater 7001F (Leica Microsystems GmbH, Germany). Bacteria adhered to coated and uncoated scaffolds were then imaged using SEM (Tescan MIRA3 FEG-SEM, Australia) at a voltage of 3 kV (spot size 11.86).

4.2.16. Statistical Analysis. A minimum of four experimental replicates (unless otherwise mentioned) were used in each study, and the results are presented as mean value \pm standard deviation. The effect of different plasma conditions as well as melimine modification in each assay compared with the controls was analyzed using two-way ANOVA (GraphPad Prism 9 software, USA). Differences between the groups were analyzed using the Tukey test of multiple comparisons, and a confidence level of $p < 0.05$ was considered as statistically significant, unless otherwise specified.

ASSOCIATED CONTENT

Supporting Information

The Supporting Information is available free of charge at <https://pubs.acs.org/doi/10.1021/acsnano.2c05812>.

Deconvolution of high-resolution C 1s spectra of control and plasma-treated surfaces under different conditions (SuppFigure 1); coomassie blue staining and wettability of melimine-modified surfaces (SuppFigure 2); ToF-SIMS spectra of secondary ions detected in pure melimine, melimine-modified surfaces, and mPCL surfaces (SuppFigure 3); elemental relative concentration of nitrogen on melimine surfaces after 3 days of incubation in PBS (SuppFigure 4); secondary ions from each amino acid residue that comprise melimine (SuppTable 1); elemental relative concentration of nitrogen on melimine surfaces after 3 days of incubation in PBS (SuppTable 2) (PDF)

AUTHOR INFORMATION

Corresponding Author

Dietmar W. Huttmacher – Faculty of Engineering, School of Mechanical, Medical and Process Engineering and Max Planck Queensland Centre, Queensland University of Technology, Brisbane, QLD 4000, Australia; Australian Research Council Training Centre for Multiscale 3D Imaging, Modelling and Manufacturing (M3D Innovation), Queensland University of Technology, Kelvin Grove, QLD 4059, Australia; Translational Research Institute, Woolloongabba, QLD 4102, Australia; Australian Research Council Industrial Transformation Training Centre in Additive Biomanufacturing and Australian Research Council Training Centre for Cell and Tissue Engineering Technologies, Queensland University of Technology, Brisbane, QLD 4059, Australia; orcid.org/0000-0001-5678-2134; Email: dietmar.huttmacher@qut.edu.au

Authors

Silvia Cometta – Faculty of Engineering, School of Mechanical, Medical and Process Engineering and Max Planck Queensland Centre, Queensland University of Technology, Brisbane, QLD 4000, Australia; Australian Research Council Training Centre for Multiscale 3D Imaging, Modelling and Manufacturing (M3D Innovation), Queensland University of Technology, Kelvin Grove, QLD 4059, Australia; orcid.org/0000-0001-8928-5337

Robert T. Jones – Central Analytical Research Facility (CARF) and Centre for Materials Science, School of Chemistry and Physics, Queensland University of Technology, Brisbane, QLD 4000, Australia; orcid.org/0000-0002-8653-0074

Alfredo Juárez-Saldivar – Unidad Académica Multidisciplinaria Reynosa Aztlán, Universidad Autónoma de Tamaulipas, Reynosa 88740, Mexico

Bogdan C. Donose – School of Information Technology and Electrical Engineering, The University of Queensland, Brisbane, QLD 4072, Australia; orcid.org/0000-0003-1935-9489

Muhammad Yasir – School of Optometry and Vision Science, University of New South Wales, Sydney, NSW 2033, Australia

Nathalie Bock – Australian Research Council Training Centre for Multiscale 3D Imaging, Modelling and Manufacturing (M3D Innovation), Queensland University of Technology, Kelvin Grove, QLD 4059, Australia; Max Planck Queensland Centre and Faculty of Health, School of Biomedical Sciences, Queensland University of Technology, Brisbane, QLD 4000, Australia; Translational Research Institute, Woolloongabba, QLD 4102, Australia

Tim R. Dargaville – Centre for Materials Science, School of Chemistry and Physics, Queensland University of Technology, Brisbane, QLD 4000, Australia; orcid.org/0000-0003-4665-9508

Karl Bertling – School of Information Technology and Electrical Engineering, The University of Queensland, Brisbane, QLD 4072, Australia; orcid.org/0000-0003-1087-2315

Michael Brünig – School of Information Technology and Electrical Engineering, The University of Queensland, Brisbane, QLD 4072, Australia; orcid.org/0000-0002-2077-0315

Aleksandar D. Rakić – School of Information Technology and Electrical Engineering, The University of Queensland, Brisbane, QLD 4072, Australia; orcid.org/0000-0002-4615-2240

Mark Willcox – School of Optometry and Vision Science, University of New South Wales, Sydney, NSW 2033, Australia; orcid.org/0000-0003-3842-7563

Complete contact information is available at:
<https://pubs.acs.org/10.1021/acsnano.2c05812>

Author Contributions

S.C. and D.W.H. conceived and designed the study. S.C. conducted all the experiments. R.T.J. performed the ToF-SIMS imaging and analysis. A.J. carried out the molecular docking analysis. B.C.D. conducted the nanoFTIR measurements and analysis. B.C.D., M.Y., N.B., T.R.D., K.B., M.B., A.D.R., M.W., and D.W.H. contributed during the evaluation of experiments and to the analysis and interpretation of the obtained data. S.C. and D.W.H. drafted the manuscript, and all authors assisted in the preparation and review of the manuscript.

Funding

This work was supported by the ARC Industrial Transformation Training Centre for Multiscale 3D Imaging, Modeling, and Manufacturing [IC 180100008], the ARC Discovery Project DP210103342, and the Max Planck Queensland Centre.

Notes

The authors declare no competing financial interest.

ACKNOWLEDGMENTS

The authors acknowledge the Central Analytical Research Facility operated by the Institute for the Future Environments (QUT) for the electron microscopy facility and the surface science laboratory where some of the data reported in this paper were obtained.

REFERENCES

- (1) Lee, M. J.; Pottinger, P. S.; Butler-Wu, S.; Bumgarner, R. E.; Russ, S. M.; Matsen, F. A. Propionibacterium Persists in the Skin despite Standard Surgical Preparation. *J. Bone Joint Surg Am.* **2014**, *96* (17), 1447–1450.
- (2) Cloutier, M.; Mantovani, D.; Rosei, F. Antibacterial Coatings: Challenges, Perspectives, and Opportunities. *Trends Biotechnol.* **2015**, *33* (11), 637–652.
- (3) Busscher, H. J.; van der Mei, H. C.; Subbiahdoss, G.; Jutte, P. C.; van den Dungen, J. J. A. M.; Zaat, S. A. J.; Schultz, M. J.; Grainger, D. W. Biomaterial-Associated Infection: Locating the Finish Line in the Race for the Surface. *Science Translational Medicine* **2012**, *4* (153), 153rv10–153rv10.
- (4) Jain, S.; Reed, M. Laminar Air Flow Handling Systems in the Operating Room. *Surg Infect (Larchmt)* **2019**, *20* (2), 151–158.
- (5) Bakhshandeh, S.; Yavari, S. A. Electrophoretic Deposition: A Versatile Tool against Biomaterial Associated Infections. *J. Mater. Chem. B* **2018**, *6* (8), 1128–1148.
- (6) Blair, J. M. A.; Webber, M. A.; Baylay, A. J.; Ogbolu, D. O.; Piddock, L. J. V. Molecular Mechanisms of Antibiotic Resistance. *Nat. Rev. Microbiol* **2015**, *13* (1), 42–51.
- (7) Campoccia, D.; Montanaro, L.; von Eiff, C.; Pirini, V.; Ravaoli, S.; Becker, K.; Arciola, C. R. Cluster Analysis of Ribotyping Profiles of Staphylococcus Epidermidis Isolates Recovered from Foreign Body-Associated Orthopedic Infections. *J. Biomed Mater. Res. A* **2009**, *88* (3), 664–672.
- (8) Concia, E.; Novelli, A.; Schito, G. C.; Marchese, A. Ideal Microbiological and Pharmacological Characteristics of a Quality

- Antimicrobial Agent: Comparing Original and Generic Molecules. *J. Chemother* **2007**, *19* (6), 609–619.
- (9) Jenkins, A.; Hills, T.; Santillo, M.; Gilchrist, M. Extended Stability of Antimicrobial Agents in Administration Devices. *J. Antimicrob. Chemother.* **2017**, *72* (4), 1217–1220.
- (10) Willcox, M. D. P.; Hume, E. B. H.; Aliwarga, Y.; Kumar, N.; Cole, N. A Novel Cationic-Peptide Coating for the Prevention of Microbial Colonization on Contact Lenses. *J. Appl. Microbiol.* **2008**, *105* (6), 1817–1825.
- (11) Dutta, D.; Cole, N.; Kumar, N.; Willcox, M. D. P. Broad Spectrum Antimicrobial Activity of Melimine Covalently Bound to Contact Lenses. *Invest. Ophthalmol. Vis. Sci.* **2013**, *54* (1), 175–182.
- (12) Yasir, M.; Dutta, D.; Willcox, M. D. P. Activity of Antimicrobial Peptides and Ciprofloxacin against *Pseudomonas Aeruginosa* Biofilms. *Molecules* **2020**, *25* (17), 3843.
- (13) Yasir, M.; Dutta, D.; Willcox, M. D. P. Enhancement of Antibiofilm Activity of Ciprofloxacin against *Staphylococcus Aureus* by Administration of Antimicrobial Peptides. *Antibiotics* **2021**, *10* (10), 1159.
- (14) Townsend, J. M.; Hukill, M. E.; Fung, K.-M.; Ohst, D. G.; Johnson, J. K.; Weatherly, R. A.; Detamore, M. S. Biodegradable Electrospun Patch Containing Cell Adhesion or Antimicrobial Compounds for Trachea Repair *in Vivo*. *Biomed. Mater.* **2020**, *15* (2), 025003.
- (15) Lin, E. M. J.; Lay, C. L.; Subramanian, G. S.; Tan, W. S.; Leong, S. S. J.; Moh, L. C. H.; Lim, K. Control Release Coating for Urinary Catheters with Enhanced Released Profile for Sustained Antimicrobial Protection. *ACS Appl. Mater. Interfaces* **2021**, *13* (49), 59263–59274.
- (16) Su, Y.; Wang, H.; Mishra, B.; Lakshmaiah Narayana, J.; Jiang, J.; Reilly, D. A.; Hollins, R. R.; Carlson, M. A.; Wang, G.; Xie, J. Nanofiber Dressings Topically Delivering Molecularly Engineered Human Cathelicidin Peptides for the Treatment of Biofilms in Chronic Wounds. *Mol. Pharmaceutics* **2019**, *16* (5), 2011–2020.
- (17) Dutta, D.; Ozkan, J.; Willcox, M. D. P. Biocompatibility of Antimicrobial Melimine Lenses: Rabbit and Human Studies. *Optom Vis Sci.* **2014**, *91* (5), 570–581.
- (18) Bendak, A.; El-Marsafi, S. M. Effects of Chemical Modifications on Polyester Fibres. *J. Islamic Acad. Sci.* **1991**, *4* (4), 275–284.
- (19) Cools, P.; Astoreca, L.; Esbah Tabaei, P. S.; Thukkaram, M.; De Smet, H.; Morent, R.; De Geyter, N. Surface Treatment of Polymers by Plasma. In *Surface Modification of Polymers: Methods and Applications*; John Wiley & Sons, Ltd: Weinheim, Germany, 2019; pp 31–65.
- (20) Vesel, A.; Mozetic, M. New Developments in Surface Functionalization of Polymers Using Controlled Plasma Treatments. *J. Phys. D: Appl. Phys.* **2017**, *50* (29), 293001.
- (21) Vesel, A.; Primc, G. Investigation of Surface Modification of Polystyrene by a Direct and Remote Atmospheric-Pressure Plasma Jet Treatment. *Materials* **2020**, *13* (11), 2435.
- (22) Hegemann, D.; Gaiser, S. Plasma Surface Engineering for Manmade Soft Materials: A Review. *J. Phys. D: Appl. Phys.* **2022**, *55* (17), 173002.
- (23) Jiang, J.; Luo, Y.; Moldgy, A.; Aranda Gonzalvo, Y.; Bruggeman, P. J. Absolute Spatially and Time-Resolved O, O₃, and Air Densities in the Effluent of a Modulated RF-Driven Atmospheric Pressure Plasma Jet Obtained by Molecular Beam Mass Spectrometry. *Plasma Processes and Polymers* **2020**, *17* (6), 1900163.
- (24) Hutmacher, D. W. Scaffolds in Tissue Engineering Bone and Cartilage. *Biomaterials* **2000**, *21* (24), 2529–2543.
- (25) Skarmoutsou, A.; Charitidis, C. A.; Gnanappa, A. K.; Tserepi, A.; Gogolides, E. Nanomechanical and Nanotribological Properties of Plasma Nanotextured Superhydrophilic and Superhydrophobic Polymeric Surfaces. *Nanotechnology* **2012**, *23* (50), S05711.
- (26) Latag, G. V.; Vasquez, M. R. Effects of RF Plasma Modification on the Thermal and Mechanical Properties of Electrospun Chitosan/Poly(Vinyl Alcohol) Nanofiber Mats. *J. Vac. Sci. Technol. B* **2018**, *36* (4), 04I101.
- (27) Chhaya, M. P.; Melchels, F. P. W.; Holzapfel, B. M.; Baldwin, J. G.; Hutmacher, D. W. Sustained Regeneration of High-Volume Adipose Tissue for Breast Reconstruction Using Computer Aided Design and Biomanufacturing. *Biomaterials* **2015**, *52*, 551–560.
- (28) Henkel, J.; Medeiros Savi, F.; Berner, A.; Fountain, S.; Saifzadeh, S.; Steck, R.; Epari, D. R.; Woodruff, M. A.; Knackstedt, M.; Schuetz, M. A.; Hutmacher, D. W. Scaffold-Guided Bone Regeneration in Large Volume Tibial Segmental Defects. *Bone* **2021**, *153*, 116163.
- (29) Chan, K. L. A.; Kazarian, S. G. New Opportunities in Micro- and Macro-Attenuated Total Reflection Infrared Spectroscopic Imaging: Spatial Resolution and Sampling Versatility. *Appl. Spectrosc.* **2003**, *57* (4), 381–389.
- (30) Lanzarotta, A. Approximating the Detection Limit of an Infrared Spectroscopic Imaging Microscope Operating in an Attenuated Total Reflection (ATR) Modality: Theoretical and Empirical Results for an Instrument Using a Linear Array Detector and a 1.5 Millimeter Germanium Hemisphere Internal Reflection Element. *Appl. Spectrosc.* **2015**, *69* (2), 205–214.
- (31) Amenabar, I.; Poly, S.; Nuansing, W.; Hubrich, E. H.; Goyadinov, A. A.; Huth, F.; Krutokhvostov, R.; Zhang, L.; Knez, M.; Heberle, J.; Bittner, A. M.; Hillenbrand, R. Structural Analysis and Mapping of Individual Protein Complexes by Infrared Nanospectroscopy. *Nat. Commun.* **2013**, *4* (1), 2890.
- (32) Mayerhöfer, T. G.; Höfer, S.; Popp, J. Deviations from Beer's Law on the Microscale – Nonadditivity of Absorption Cross Sections. *Phys. Chem. Chem. Phys.* **2019**, *21* (19), 9793–9801.
- (33) Rasul, R.; Cole, N.; Balasubramanian, D.; Chen, R.; Kumar, N.; Willcox, M. D. P. Interaction of the Antimicrobial Peptide Melimine with Bacterial Membranes. *Int. J. Antimicrob. Agents* **2010**, *35* (6), 566–572.
- (34) Taylor, M. J.; Aitchison, H.; Hawker, M. J.; Mann, M. N.; Fisher, E. R.; Graham, D. J.; Gamble, L. J. Time of Flight Secondary Ion Mass Spectrometry—A Method to Evaluate Plasma-Modified Three-Dimensional Scaffold Chemistry. *Biointerphases* **2018**, *13* (3), 03B415.
- (35) Baio, J. E.; Graham, D. J.; Castner, D. G. Surface Analysis Tools for Characterizing Biological Materials. *Chem. Soc. Rev.* **2020**, *49* (11), 3278–3296.
- (36) Chen, R.; Willcox, M. D. P.; Cole, N.; Ho, K. K. K.; Rasul, R.; Denman, J. A.; Kumar, N. Characterization of Chemosensitive Surface Attachment of the Cationic Peptide Melimine and Its Effects on Antimicrobial Activity. *Acta Biomater* **2012**, *8* (12), 4371–4379.
- (37) Desmet, T.; Poleunis, C.; Delcorte, A.; Dubruel, P. Double Protein Functionalized Poly-ε-Caprolactone Surfaces: In Depth ToF-SIMS and XPS Characterization. *J. Mater. Sci: Mater. Med.* **2012**, *23* (2), 293–305.
- (38) Tortora, L.; Concolato, S.; Urbini, M.; Giannitelli, S. M.; Basoli, F.; Rainer, A.; Trombetta, M.; Orsini, M.; Mozetic, P. Functionalization of Poly(ε-Caprolactone) Surface with Lactose-Modified Chitosan via Alkaline Hydrolysis: ToF-SIMS Characterization. *Biointerphases* **2016**, *11* (2), 02A323.
- (39) Chen, M.; Besenbacher, F. Light-Driven Wettability Changes on a Photoresponsive Electrospun Mat. *ACS Nano* **2011**, *5* (2), 1549–1555.
- (40) John, T.; Abel, B.; Martin, L. L. The Quartz Crystal Microbalance with Dissipation Monitoring (QCM-D) Technique Applied to the Study of Membrane-Active Peptides. *Aust. J. Chem.* **2018**, *71* (7), 543.
- (41) Shard, A. G. Detection Limits in XPS for More than 6000 Binary Systems Using Al and Mg K α X-Rays. *Surf. Interface Anal.* **2014**, *46* (3), 175–185.
- (42) Costa, F.; Carvalho, I. F.; Montelaro, R. C.; Gomes, P.; Martins, M. C. L. Covalent Immobilization of Antimicrobial Peptides (AMPs) onto Biomaterial Surfaces. *Acta Biomaterialia* **2011**, *7* (4), 1431–1440.
- (43) Onaizi, S. A.; Leong, S. S. J. Tethering Antimicrobial Peptides: Current Status and Potential Challenges. *Biotechnol. Adv.* **2011**, *29* (1), 67–74.
- (44) Yasir, M.; Dutta, D.; Hossain, K. R.; Chen, R.; Ho, K. K. K.; Kuppasamy, R.; Clarke, R. J.; Kumar, N.; Willcox, M. D. P.

Mechanism of Action of Surface Immobilized Antimicrobial Peptides Against *Pseudomonas Aeruginosa*. *Front. Microbiol.* **2020**, *10*, 3053.

(45) Chen, Q.; Liu, D.; Gong, Y.; Xiao, Q.; Li, Z. Modification of Titanium Surfaces via Surface-Initiated Atom Transfer Radical Polymerization to Graft PEG-RGD Polymer Brushes to Inhibit Bacterial Adhesion and Promote Osteoblast Cell Attachment. *J. Wuhan Univ. Technol.-Mater. Sci. Ed.* **2017**, *32* (5), 1225–1231.

(46) Bartnikowski, M.; Abdal-hay, A.; Bartnikowski, N. J.; Kyoung Kim, Y.; Ivanovski, S. A Comprehensive Study of Acid and Base Treatment of 3D Printed Poly(ϵ -Caprolactone) Scaffolds to Tailor Surface Characteristics. *Appl. Surf. Sci.* **2021**, *555*, 149602.

(47) Huth, F.; Govyadinov, A.; Amarie, S.; Nuansing, W.; Keilmann, F.; Hillenbrand, R. Nano-FTIR Absorption Spectroscopy of Molecular Fingerprints at 20 Nm Spatial Resolution. *Nano Lett.* **2012**, *12* (8), 3973–3978.

(48) Claus, T. K.; Richter, B.; Hahn, V.; Welle, A.; Kayser, S.; Wegener, M.; Bastmeyer, M.; Delaittre, G.; Barner-Kowollik, C. Simultaneous Dual Encoding of Three-Dimensional Structures by Light-Induced Modular Ligation. *Angew. Chem., Int. Ed.* **2016**, *55* (11), 3817–3822.

(49) Lamiable, A.; Thévenet, P.; Rey, J.; Vavrusa, M.; Derreumaux, P.; Tufféry, P. PEP-FOLD3: Faster de Novo Structure Prediction for Linear Peptides in Solution and in Complex. *Nucleic Acids Res.* **2016**, *44* (W1), W449–454.

(50) McNutt, A. T.; Francoeur, P.; Aggarwal, R.; Masuda, T.; Meli, R.; Ragoza, M.; Sunseri, J.; Koes, D. R. GNINA 1.0: Molecular Docking with Deep Learning. *Journal of Cheminformatics* **2021**, *13* (1), 43.

(51) Salentin, S.; Schreiber, S.; Haupt, V. J.; Adasme, M. F.; Schroeder, M. PLIP: Fully Automated Protein-Ligand Interaction Profiler. *Nucleic Acids Res.* **2015**, *43* (W1), W443–447.